Density distribution of ^{17}Ne and possible shell-structure change in the proton-rich *sd*-shell nuclei

K. Tanaka,[1,*] M. Fukuda,[1] M. Mihara,[1] M. Takechi,[1,*] D. Nishimura,[1] T. Chinda,[1] T. Sumikama,[1,†] S. Kudo,[1] K. Matsuta,[1] T. Minamisono,[1,‡] T. Suzuki,[2,§] T. Ohtsubo,[2] T. Izumikawa,[3] S. Momota,[4] T. Yamaguchi,[5,§] T. Onishi,[5] A. Ozawa,[5,‖] I. Tanihata,[5,¶] and T. Zheng[5,**]

[1]*Department of Physics, Osaka University, Toyonaka, Osaka 560-0043, Japan*
[2]*Department of Physics, Niigata University, Niigata, Niigata 950-2181, Japan*
[3]*RI Center, Niigata University, Niigata, Niigata 951-8510, Japan*
[4]*Kochi University of Technology, Tosayamada, Kochi 782-8502, Japan*
[5]*RIKEN Nishina Center, Wako, Saitama 351-0198, Japan*

(Received 6 October 2009; revised manuscript received 12 May 2010; published 13 October 2010)

Reaction cross sections (σ_R) for the proton drip-line nucleus ^{17}Ne have been measured on ^{9}Be, ^{12}C, and ^{27}Al targets at 64 and 42 MeV/nucleon by the transmission method. From the energy dependence of the σ_R including the high energy data, the density distribution of ^{17}Ne was deduced through a modified Glauber-type calculation. It is indicated that ^{17}Ne has a long tail in the density, consistent with a $(2s_{1/2})^2$-dominant configuration of two valence protons.

DOI: 10.1103/PhysRevC.82.044309 PACS number(s): 21.10.Gv, 25.60.Dz, 27.20.+n

I. INTRODUCTION

^{17}Ne($I^\pi = 1/2^-$, $T_{1/2} = 109.2$ ms) is an interesting candidate for a two-proton halo nucleus. Since the Coulomb barrier prevents proton-halo formation, the number of known halo nuclides on the proton-rich side is less than that on the neutron-rich side. Only for ^{8}B, with a weakly bound valence proton, is there clear evidence for a long tail in the density distribution [1–4]. ^{17}Ne has a Borromean structure, in which none of its (^{15}O + p + p) subsystems forms a bound state, and the two valence protons are weakly bound ($S_{2p} = 0.93$ MeV). Because the two valence protons of ^{17}Ne are considered to be in the *sd*-shell, their radial wave functions exhibit configuration mixing of the s and d orbitals. If they had a d-dominant configuration, a centrifugal barrier would hinder the radial extension of the wave function.

Early experimental studies of ^{17}Ne suggested a possible halo structure for ^{17}Ne. The interaction cross sections (σ_I) for ^{17}Ne at relativistic energies were found to be larger than those for the mirror nucleus ^{17}N, though σ_I for the nuclei of other mirror pairs including proton-drip line nuclei with $Z = 4 \sim 10$ are almost the same for both nuclei in the mirror pair [5]. Moreover, the asymmetry of β-decay probabilities between the $A = 17$ mirror pair of ^{17}Ne and ^{17}N is larger than those of other mirror pairs, implying an abnormal nuclear structure of the initial and/or final state [6].

Subsequent intensive theoretical and experimental studies gave conflicting results. Measurements by Warner *et al.* of the σ_R for ^{17}Ne on a Si target around 40 MeV/nucleon [7], suggested that ^{17}Ne is not so large as other neutron halo nuclei. However the comparatively narrow width of the longitudinal momentum distribution of the projectile fragments and the large two-proton removal cross section (σ_{-2p}) for ^{17}Ne measured by Kanungo *et al.* [8,9], suggest the possibility of a halo structure. The recent measurement of charge radius of ^{17}Ne supports the existence of a tail in the proton distribution [10].

The results of theoretical studies on ^{17}Ne are also controversial. The structure of ^{17}Ne calculated by Timofeyuk *et al.* with a three-cluster model has a $(2s_{1/2})^2$-dominant configuration [11]. However a three-body model calculation by Garrido *et al.* suggested almost equal occupation probabilities of the $(2s_{1/2})^2$ and $(1d_{5/2})^2$ levels [12,13]. From the Coulomb mass shift, Nakamura *et al.* suggested a $(2s_{1/2})^2$ dominance [14], however Fortune *et al.* suggested a $(1d_{5/2})^2$ dominance [15,16]. Kitagawa *et al.* also proposed a $(1d_{5/2})^2$ dominance through calculations of the σ_I with a Hartree-Fock type wave function and the Glauber model [17].

In the present study, there is additional interest in relation to the new magic number 16. For some *sd*-shell nuclei on the neutron-rich side close to the drip line, the shell structure changes such that the $1d_{3/2}$ level energy increases [18] and $2s_{1/2}$ level energy decreases compared with those of stable nuclei, which leads to the magic number 16 [19]. When the $2s_{1/2}$ level is lowered in energy, a level inversion of $2s_{1/2}$ and $1d_{5/2}$ can occur. In such a case for ^{17}Ne, a larger $2s_{1/2}$ component in the proton configuration can be expected, which can lead to a halo formation. In contrast, because the Coulomb barrier impedes a shift of the $2s_{1/2}$ level, this new magic number 16 might not emerge in proton-rich nuclei. To date, few studies of the new magic number in the vicinity of the

*Present address: RIKEN Nishina Center, Wako, Saitama 351-0198, Japan.
†Present address: Faculty of Science and Technology, Tokyo University of Science, Noda, Chiba 278-8510, Japan.
‡Present address: Department for the Application of Nuclear Technology, Fukui University of Technology, Fukui 910-8505, Japan.
§Present address: Department of Physics, Saitama University, Saitama 338-8570, Japan.
‖Present address: Department of Physics, Tsukuba University, Tsukuba, Ibaraki 305-8571, Japan.
¶Present address: Research Center for Nuclear Physics (RCNP), Osaka University, Ibaraki, Osaka 567-0047, Japan.
**Present address: School of Physics and State Key Laboratory of Nuclear Physics and Technology, Peking Univerisity, Beijing 100871, P.R. China.

proton-drip line have been carried out, and thus it has not been confirmed experimentally on the proton-rich side. A study of the ^{17}Ne nucleus would help to elucidate the mechanism related to the new magic number 16 in proton-rich nuclei.

In order to solve the structure questions noted above, we studied the nucleon density distribution of ^{17}Ne through σ_R. The σ_R were measured at several tens of MeV/nucleon because the cross section is more sensitive to the dilute density part at these energies than at higher energies. The density distribution can be deduced from the energy dependence of σ_R, including the high energy σ_I data, by using a modified Glauber-type calculation. With these results, we can address the question of the structure of ^{17}Ne.

II. EXPERIMENT

We measured the σ_R for ^{17}Ne on ^{9}Be, ^{12}C, and ^{27}Al reaction targets at 64 and 42 MeV/nucleon using the transmission method. The nucleon-nucleon total cross section (σ_{NN}) is, respectively, about two times greater at 64 MeV/nucleon and three times greater at 42 MeV/nucleon than at relativistic energies [20]. The experiment was carried out at the RIKEN accelerator research facility. A 135 MeV/nucleon ^{20}Ne primary beam with an intensity of 10 pnA was delivered from the RIKEN ring cyclotron (RRC), and was directed onto ^{9}Be production targets with 2–9 mm thicknesses depending on the required secondary beam energy. The secondary ^{17}Ne beam was separated from other reaction products in the RIKEN projectile-fragment separator (RIPS) [21]. Wedge type aluminum energy degraders with a central thickness of 1099 mg/cm^2, a wedge angle of 6.1 mrad, or a 583 mg/cm^2–3.1 mrad one were used at the momentum dispersive focus F1 of RIPS. The typical intensity of the ^{17}Ne beam was 100 cps and the purity was ∼10%. The main contaminant in the secondary beam was ^{15}O.

Figure 1 shows a schematic drawing of the experimental setup located at the final focus F3 of RIPS. Before the reaction target mounted at the F3 focus, three parallel-plate avalanche counters (PPAC) [22] and two silicon detectors (Si) were installed. The particles were identified by the magnetic rigidity at D2 ($B\rho$), the time-of-flight (TOF) measured using PPACs and the RF signal from RRC, and the ΔE of the two Si detectors at F3 with dimensions 100 μm × 30 × 30 mm^2. From the

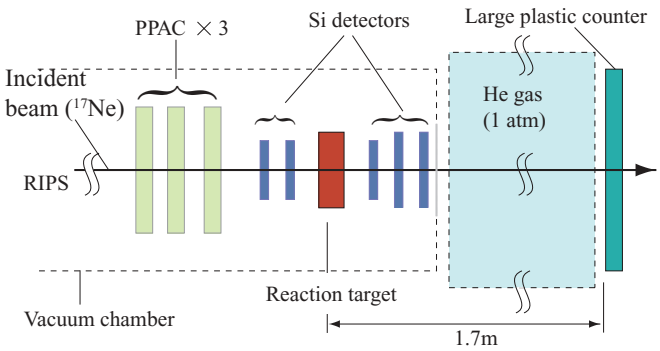

FIG. 1. (Color online) Experimental setup around the reaction target.

correlation of the two Si spectra, mis-identifications due to channeling events were greatly reduced.

TOF and ΔE were sufficient for particle identification after the reaction target. Because ^{17}Ne is a proton drip-line nucleus, particles can be identified by knowing only the atomic number. The experimental setup for the identification after the target was similar to that of Ref. [4]. We measured TOF between the PPACs before the target and a large plastic counter installed about 1.7 m downstream of the target and ΔE in the three Si detectors installed just behind the target. The large plastic counter was 3 × 600 × 600 mm^3 which covered a large enough solid angle to detect scattered ^{17}Ne beam due to elastic or multiple scatterings in the reaction target. The first Si detector behind the target was 100 μm ×30 × 30 mm^2 in size, and that of other two detectors were 200 μm × 50 × 50 mm^2.

In the particle identification spectrum before the target, the background ratio in the ^{17}Ne peak was less than 10^{-5} which is small enough to deduce σ_R. From TOF and ΔE after the target, the atomic number Z can be determined. Because ^{17}Ne is a proton drip-line nucleus, a neutron removal implies a change of Z, and therefore the Z identification was enough to discriminate the nonreacted beam from reaction products. To correct for reactions outside the target, mainly in the Si detectors after the target and in the large plastic counter, we also carried out a target-out measurement, in which the incident beam energy at the first Si detector after the target was adjusted to be the same as that in the target-in measurement.

III. RESULTS

Figure 2(A) shows a typical particle-identification spectrum after the reaction target for the target-in measurement and Fig. 2(B) for the target-out measurement. In Fig. 2(A), ^{17}Ne is clearly separated from all other reaction products. The upper tail of the ^{17}Ne peak with a constant ΔE was caused by nuclear reactions in the materials behind the Si detectors such as the vacuum window or He gas. The upper-right tail of the ^{17}Ne peak corresponds to inelastic scattering events in the target.

Because the ^{17}Ne does not have any excited states, the inelastic scattering events shown in the figure are due to a transfer of energy to the target nucleus. Figure 3 shows a spectrum of energy transferred to the target nucleus deduced from the TOF spectrum of ^{17}Ne after the reaction target of ^{9}Be for 64 MeV/nucleon setting. Though some inelastic events are included in the unreacted ^{17}Ne peak, they must be counted as inelastic reaction events. This was done by the following method. The main peak was fitted with a Gaussian function and the tail part with an exponential curve. Point O is the zero energy point on the horizontal axis which corresponds to the center of the Gaussian. Point A is defined as the zero energy point on the exponential curve. Point B is defined as the intersection of the Gaussian and the exponential curve. Point C is a projection of B on the horizontal axis. Then the area below the exponential curve from A to B, as shown by the hatched area in Fig. 3, was defined as the upper limit of the inelastic-scattering correction. Additionally, a line is drawn between O and B (dashed line in Fig. 3), and the area under the line integrated from O to B, as shown by the shaded area in Fig. 3, was defined as the lower limit of the correction.

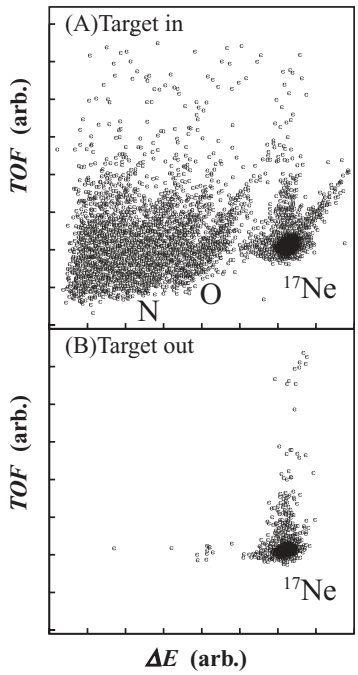

FIG. 2. Typical particle identification spectra after the ^{9}Be reaction target for the target-in (A) and target-out (B) measurements with the ^{17}Ne beam at 64 MeV/nucleon.

The correction was defined as an average of the upper and lower limits and the error was given as the difference between the correction value and the upper (or lower) limit. In this study, the amplitude of the tail is not large enough to provide an accurate exponential fit, and thus there is a non-negligible ambiguity in the slope. The systematic error due to this ambiguity was included in the total error of the experimental results.

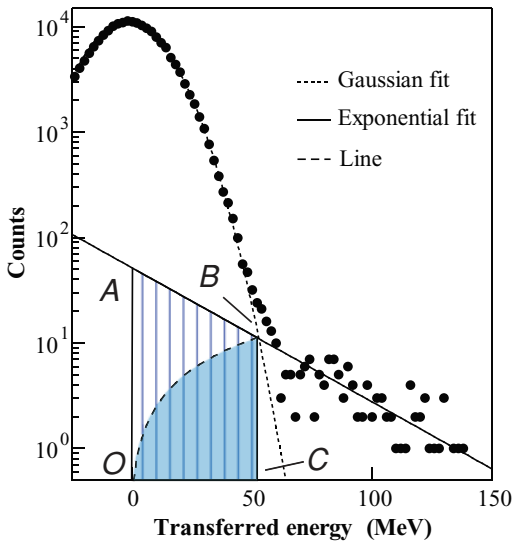

FIG. 3. (Color online) Typical transferred-energy spectrum for ^{17}Ne beam at 64 MeV/nucleon with a ^{9}Be target, for the inelastic-scattering correction. The hatched area shows the upper limit of the inelastic-scattering correction and the shaded area the lower limit.

TABLE I. Experimental results for σ_R and σ_I obtained in the present study. The σ_I at higher energies utilized to deduce the density distribution are also shown.

Projectile	Target	Energy (MeV/nucleon)	σ_R (mb)	σ_I (mb)
^{12}N	Be	69	1089 ± 26	1032 ± 25
		46	1258 ± 23	1182 ± 22
^{13}O	Be	76	1120 ± 13	1090 ± 12
		52	1262 ± 29	1203 ± 28
^{17}Ne	Be	700		968 ± 45[a]
		64	1265 ± 22	1215 ± 14
		42	1493 ± 40	1380 ± 32
	C	680		1090 ± 76[a]
		620		1044 ± 31[a]
		64	1336 ± 22	1302 ± 19
		42	1519 ± 68	1422 ± 22
	Al	670		1412 ± 224[a]
		64	1831 ± 49	1759 ± 23
		43	2032 ± 48	1893 ± 37

[a]Measured by Ozawa *et al* [5].

The σ_R is deduced as follows:

$$\sigma_R = -\frac{1}{t} \ln \left(\frac{R_{\text{in}}}{R_{\text{out}}} \right), \tag{1}$$

where t denotes the thickness of reaction target, R_{in} is the ratio of the number of outgoing ^{17}Ne particles to that of incident ^{17}Ne for the target-in measurement, and R_{out} the same ratio for the target-out measurement. The σ_R for ^{12}N, ^{13}O and ^{17}Ne measured in this study are summarized in Table I. The beam energies indicated in Table I are mean energies in the targets calculated as

$$E_{\text{beam}} = \frac{1}{t} \int_{E_i}^{E_o} E \frac{dx}{dE} dE, \tag{2}$$

where E_{beam} is the mean energy in a target, E_i is the incident beam energy and E_o the beam energy at exit from the target.

The present experimental results are summarized in Table I. The main source of the errors of σ_R is the statistical error. The systematic error in estimating the amount of inelastic scattering events increases the total error a little. The results for the interaction cross section (σ_I) are also listed in the table. The σ_I is the nuclide-changing cross section which can be represented as $\sigma_I = \sigma_R - \sigma$(inelastic scattering). Table I also includes the data from Ref. [5] obtained at high energies where σ_I and σ_R are considered to be almost the same, which are used in the analyses described later.

In Fig. 4, the σ_R from the present experiment are compared with those calculated with the semiempirical formula which reproduces σ_R for stable nuclei proposed by Kox *et al.* [23]. The σ_R for ^{17}Ne, shown as the ratio to the calculated σ_R, are larger than those for the stable nucleus ^{12}C [24] by more than 10%.

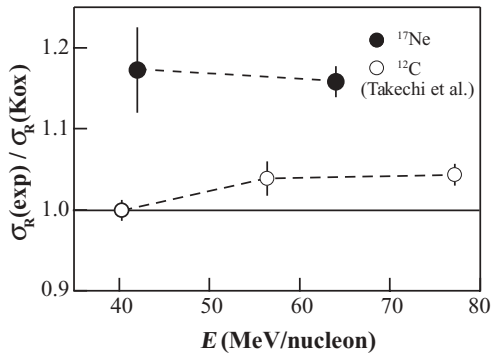

FIG. 4. The ratio of the measured σ_R on the ^{12}C target to the σ_R calculated with the Kox empirical formula, plotted as a function of energy. The closed circles correspond to the data of ^{17}Ne measured in the present study. The open circles indicate those of the stable nucleus ^{12}C measured by Takechi *et al.* [24]. The dashed lines are to guide the eye.

IV. ANALYSIS AND DISCUSSION

A. Glauber-type calculation

The σ_R can be connected with a nucleon density distribution through a Glauber-type calculation. The optical limit approximation of the Glauber calculation (OLA) is a basic and useful method to calculate σ_R, though it has an inaccuracy for nuclei having a dilute density part like a halo because the multiple scattering effect (or few-body effect) is not taken into account in this method [25]. Therefore, we adopted the modified optical limit approximation (MOL), an improvement proposed by Abu-Ibrahim and Suzuki [25]. Additionally, Takechi *et al.* successfully included the Fermi-motion effect in the MOL as a low energy correction [24] because these models are designed to be used at relativistic energies. With this improved MOL calculation, we deduced the nucleon density distribution of ^{17}Ne through χ^2 fits to the experimental σ_R, adopting several different density shapes.

The Glauber-type calculation used in the present study to deduce nucleon density distributions is described in detail in Refs. [24,26], and formulated as follows. The σ_R is calculated as

$$\sigma_R = 2\pi \int db\, b[1 - T(b)]C(E), \tag{3}$$

where $C(E)$ denotes the Coulomb effect that includes only the bending of trajectory of the projectile [4]. $T(b)$ denotes the transmission probability at an impact parameter b. In the MOL calculation, $T(b)$ is expressed as [26]

$$T(b)^{MOL} = \exp\left\{-\int d\boldsymbol{s}\rho_z^P(\boldsymbol{s})\left(1-\exp\left[\int d\boldsymbol{t}\rho_z^T(\boldsymbol{t})\sigma_{NN} \times\Gamma(\boldsymbol{b}+\boldsymbol{s}-\boldsymbol{t})\right]\right)\right\}\exp\left\{-\int d\boldsymbol{t}\rho_z^T(\boldsymbol{t}) \times\left(1-\exp\left[\int d\boldsymbol{s}\rho_z^P(\boldsymbol{s})\sigma_{NN}\Gamma(\boldsymbol{b}+\boldsymbol{t}-\boldsymbol{s})\right]\right)\right\}, \tag{4}$$

where ρ_z^P, ρ_z^T are the z (beam direction)-integrated densities of the projectile and the target nuclei, respectively, Γ the nucleon-nucleon profile function, $\boldsymbol{s}$ and $\boldsymbol{t}$ the nucleon coordinates of the projectile and the target in the plane perpendicular to the beam axis. In this formulation, similarly to the OLA, σ_R can be calculated uniquely with the three inputs, σ_{NN}, projectile and target densities without free parameters. Among the inputs, only the projectile density is unknown because the σ_{NN} and target density can be taken from the precise experimental data.

In the intermediate energy region, OLA underestimates σ_R compared with the experimental value ($\sigma_R^{\rm exp}$) even for the stable nuclei [4]. To improve the accuracy of the Glauber-type calculation, Takechi *et al.* measured σ_R precisely for the stable nucleus ^{12}C on ^{9}Be, ^{12}C, and ^{27}Al targets [24] and proposed to incorporate the Fermi-motion effect into MOL calculations. They assumed the effective σ_{NN} based on the momentum distribution of valence nucleons with the Goldhaber model. The effective σ_{NN} in a nucleus is described as

$$\sigma_{NN}^{\rm eff} = \int_{-\infty}^{\infty} dp_{\rm rel}\sigma_{NN}D(p_{\rm rel}), \tag{5}$$

where the function of momentum distribution $D(p_{\rm rel})$ is expressed with relative momentum between nucleons ($p_{\rm rel}$) in the projectile and the target as

$$D(p_{\rm rel}) = \frac{1}{\sqrt{2\pi\left(\langle p_P^2\rangle + \langle p_T^2\rangle\right)}} \times \exp\left[-\frac{(p_{\rm rel}-p_{\rm proj})^2}{2\sqrt{\langle p_P^2\rangle + \langle p_T^2\rangle}}\right]. \tag{6}$$

In this equation, $p_{\rm proj}$ denotes the momentum of a nucleon with the same velocity as the projectile, $\langle p_P^2\rangle$ a mean square momentum of a nucleon in the projectile and $\langle p_T^2\rangle$ that in the target. For stable nuclei, we employed the averaged experimental value of 90 MeV/c as $\sqrt{\langle p_T{}^2\rangle}$. For ^{17}Ne, the ρ^P in Eq. (4) was divided into a core and two valence nucleons part. For the core part we used the experimental value of momentum width from the data for ^{15}O (= 81 MeV/c) [27], and for the valence part the data for ^{17}Ne (= 51 MeV/c) [8].

B. Nucleon density distribution of ^{17}Ne

Because the shape of the density distribution is restricted by the functional shape chosen, it is important to test several shapes to deduce a reliable density distribution of the nucleus of interest. Using MOL with the Fermi-motion correction, proposed by Takechi *et al.* [24], the best-fit density distributions were deduced by optimizing the parameters in the density functions through a χ^2-fitting procedure to reproduce the experimental σ_R for ^{17}Ne. The error in the density for ^{17}Ne was determined by summing the error ranges for each density function. The σ_R data used for the fitting procedure were the present σ_R and the $\sigma_{\rm I}$ data at high energies [5]. These data are summarized in Table I.

The density function was divided into a core and a valence part. In this study, the harmonic oscillator type function (HO) which is often used as the density shape for light stable nuclei was used in each case as the core shape. The HO type function

for the core part is expressed as

$$\rho_c^i(r) = \rho_{c0}^i \times \left(1 + \frac{C-2}{3}\left(\frac{r}{b}\right)^2\right) \exp\left(-\left(\frac{r}{b}\right)^2\right), \quad (7)$$

where i denotes the proton or neutron and C is the number of protons (Z_c) or neutrons (N_c) in the core. The b is the core width parameter and ρ_{c0} is the normalization factor. The same width was used for the proton- and neutron-core densities. In the case of ^{17}Ne, we assumed ^{15}O ($Z_c = 8$, $N_c = 7$) as the core nucleus because ^{16}F is unbound. For neutrons in ^{17}Ne, only the core part was assumed because of their larger binding energies.

For the valence part of protons in ^{17}Ne, we tested several functions, while only the core part was assumed for neutrons. The functions tested for valence protons are: a square of the Yukawa (Yukawa-type) function, a single particle model (SPM) function, and a HO function. The functional shapes of the Yukawa and the SPM densities extend to long distance. In contrast, the HO shape does not have a long-distance component. By using these functions with different properties, the density shape of ^{17}Ne was reliably deduced. The results for each shape of the density function for valence protons are discussed below.

1. *HO + Yukawa-type density*

The square of the Yukawa function is a good function to approximate the shape of the surface density not only for the orbital angular momentum $\ell = 0$ case but also for the $\ell \neq 0$ cases in which the centrifugal barriers exist [4]. It is useful because of its simplicity and independence from the details of nuclear structure [4,28–32]. The Yukawa-type nucleon density function is defined as follows:
for protons

$$\rho^p(r) = \begin{cases} X \times \rho_c^p(r) & r \leqslant r_c \\ Y \times \dfrac{\exp(-\lambda r)}{r^2} & r > r_c, \end{cases} \quad (8)$$

for neutrons

$$\rho^n(r) = \rho_c^n(r). \quad (9)$$

Here r_c is the intersection point of the core and the tail part, λ the tail slope, and X and Y the amplitude of the core and the tail part, respectively. Free parameters in these functions are the core width b of the HO type function, the tail slope λ, and the relative tail amplitude Y/X.

Figure 5 shows the density distribution of ^{17}Ne deduced using the Yukawa-type function. The best-fit density is shown by the thick solid curve and the shaded area shows the experimental error which does not include the systematic effect in the calculation. The reduced χ^2 for the best-fit curve is 0.95, which shows this function is quite suitable for representing the nucleon density of ^{17}Ne. The best-fit parameters were $b = 1.54$ fm, $Y/X = 16.8$, and $\lambda = 0.80$ (fm^{-1}) for this type of density. In Fig. 5, a clear tail in the density can be seen. In order to test the need for this tail in the model function, we tried to use the HO type core only as a trial function. As shown in Table II, the best-fit χ^2 for this HO-only function is considerably larger than that in the case of the (HO + Yukawa-type) function, indicative of the need to include a tail in the density.

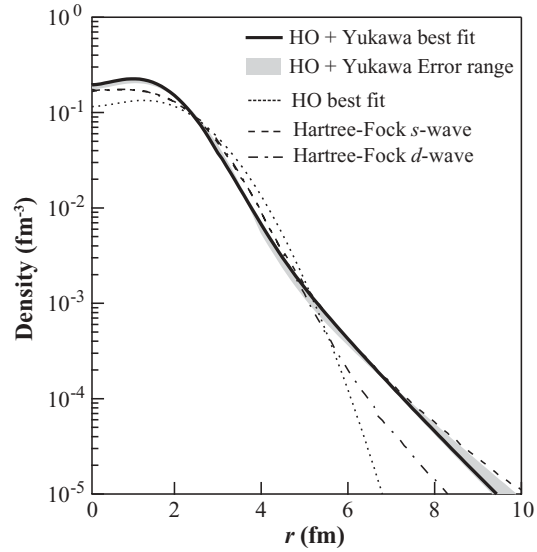

FIG. 5. Density distributions of ^{17}Ne deduced with the fitting procedure using (HO + Yukawa-type) density function. The thick-solid line denotes the best-fit density and the shaded area indicates the error. The dotted line shows the best-fit density with HO function only. The dashed- and dot-dashed lines show the theoretical densities calculated with Hartree-Fock model with $(2s_{1/2})^2$ and $(1d_{5/2})^2$ configurations, respectively [17].

In Fig. 5, these fitted densities are compared with theoretical densities calculated by Kitagawa *et al.* with the modified Hartree-Fock model [17]. The tail parts of these theoretical distributions are based on the $(2s_{1/2})^2$ or $(1d_{5/2})^2$ proton configurations for which the proton binding energy is assumed to be half of the experimental S_{2p} of ^{17}Ne. The tail part of the deduced distribution is in good agreement with the theoretical $(2s_{1/2})^2$ distribution, especially in the $r = 5 \sim 8$ fm region.

2. *HO + single particle model density*

The density distribution by the SPM is more realistic than that of the Yukawa type in the tail region, because it takes into account the Coulomb and the centrifugal barrier effects which are not explicitly included in the Yukawa-type function. The amplitude of the density of the two valence protons should be normalized to two, which introduces a certain restriction in this SPM, in contrast to the case of a Yukawa-type function.

In this SPM, the wave function of the two valence protons was calculated by solving the Schrödinger equation numerically, assuming the Woods-Saxon potential, the Coulomb barrier, and the centrifugal barrier. The nuclear part of the

TABLE II. Result of the χ^2 fitting for ^{17}Ne. The χ^2 and the width parameter for the fits with an HO core part only are compared to those with the (HO+Yukawa) function.

	Reduced χ^2	Total χ^2	HO Width
HO + Yukawa	0.95	6.65	1.54
HO	2.3	16.1	1.92

potential assumed is written as

$$V = \left(-V_0 + V_1(l \cdot s)\frac{r_{l\cdot s}^2}{r}\frac{d}{dr}\right)\left[1 + \exp\left(\frac{r - R_c}{a}\right)\right]^{-1}, \tag{10}$$

where $a(= 0.6$ fm) is the diffuseness parameter, $R_c(= r_0 A^{1/3}$, $r_0 = 1.2$ fm) the radius of the Woods-Saxon potential, $r_{l\cdot s}$ ($= 1.1$ fm) the radius for spin-orbit potential, and $V_1(=$ 17 MeV) is the $l \cdot s$ strength, taken from [33]. The depth of this potential (V_0) was adjusted to reproduce the experimental binding energy of a valence proton. For ^{17}Ne we cannot use the binding energy of a single valence proton (S_p) because ^{16}F is not a bound nucleus. Therefore, we assumed that two valence protons are bound independently on the ^{15}O core. In this case, S_p is a free parameter and is assumed to be in a range from $\sim$0 MeV to the two-proton binding energy ($S_{2p} = 0.93$ MeV). In this model, the $\rho(r)$ of ^{17}Ne consists of the HO-type core and the two valence protons calculated with the SPM. The core widths for protons and for neutrons were assumed to be the same. Since the effect of the spin-orbit potential in Eq. (10) on the wave function is not so large, the $\rho(r)$ assuming $d_{5/2}$ as a valence proton orbital and that assuming $d_{3/2}$ are almost the same. Therefore, we considered a configuration mixing of $2s_{1/2}$ and $1d_{5/2}$ for the two valence protons in ^{17}Ne as follows:

$$\phi(r) = \left\{\sqrt{\alpha}\phi_{[(2s_{1/2})^2]}(r) + \sqrt{1-\alpha}\,\phi_{[(1d_{5/2})^2]}(r)\right\}, \tag{11}$$

where α denotes the occupation probability of the $(2s_{1/2})^2$ configuration. The free parameters in this model are the core width b, the binding energy S_p and α. Thus the (HO + SPM) function is defined as
for protons

$$\rho^p(r) = \rho_c^p(r) + |\phi(r)|^2, \tag{12}$$

for neutrons

$$\rho^n(r) = \rho_c^n(r). \tag{13}$$

Figure 6 shows the deduced density distribution of ^{17}Ne with the (HO + SPM) function. The deduced $\rho(r)$ with (HO + SPM) function is also in good agreement with the theoretical curve with the proton $(2s_{1/2})^2$ configuration. Figure 7 shows the total χ^2 with the SPM function as a function of s-orbital occupancy α. Each line corresponds to a different S_p from 0.1 MeV to 0.93 MeV ($= S_{2p}$). At each plotted point, the width of core b was optimized. The best-fit parameters for (HO + SPM) density are $b = 1.62$ fm, $S_p = 0.7$ MeV, and $\alpha = 1.0$. The reduced χ^2 is 1.00. The error ranges indicated by the shaded area in Fig. 7 are based on the χ^2 minimum among all the three types of density model in this study. Though we did the parameter optimization by calculations at limited lattice points on the $S_p - \alpha$ plane as shown in Fig. 7, this does not affect the result seriously due to the fairly large error range shown in this figure. From the error range in Fig. 7 with $S_p = 0.1 \sim 0.93$ MeV, the s-orbital occupancy α was obtained as $\alpha = 1.0^{+0.0}_{-0.55}$. This whole error range is covered by the deduced $\rho(r)$ in Fig. 6, though the error of $\rho(r)$ in this figure does not appear to be large. This is because the effects on $\rho(r)$ of the parameters α and S_p compensate for one another. The modified HF calculation assuming the $(2s_{1/2})^2$ configuration and the single proton binding energy of $S_p = S_{2p}/2$, reproduces the deduced density distribution very well, especially at the tail region.

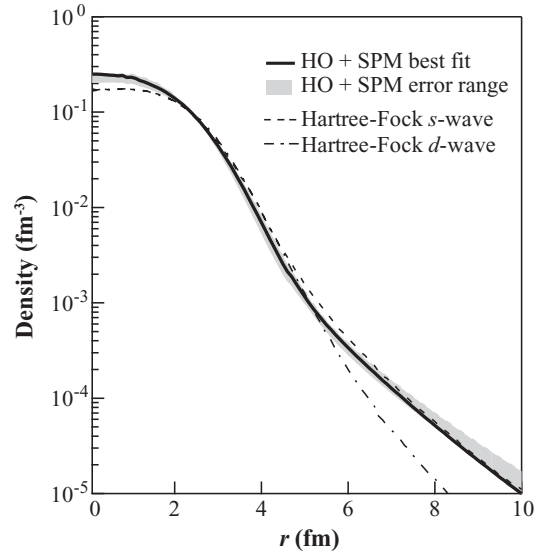

FIG. 6. Density distribution of ^{17}Ne deduced with the fitting procedure assuming an (HO + SPM) density function. The thick-solid line denotes the best-fit density and the shaded area indicates the error. The other lines show the same theoretical calculations as in Fig. 5.

3. *HO + HO density*

In order to test the model dependence of the deduced density distribution, especially on the necessity for including the tail, a harmonic-oscillator (HO) type function which does not have a long tail was tested as an alternative valence two proton function. The (HO + HO) function of the proton density is

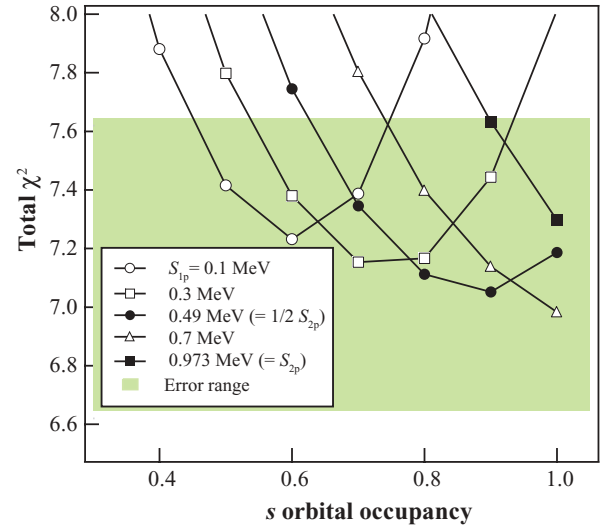

FIG. 7. (Color online) Total χ^2 map plotted against α with the (HO + SPM) density. Each plot shows deduced χ^2 with fixed S_p parameter in the (HO + SPM) density. Lines are guides for eyes only. The error range shown by shaded area is based on the results with all types of density function considered in the present study.

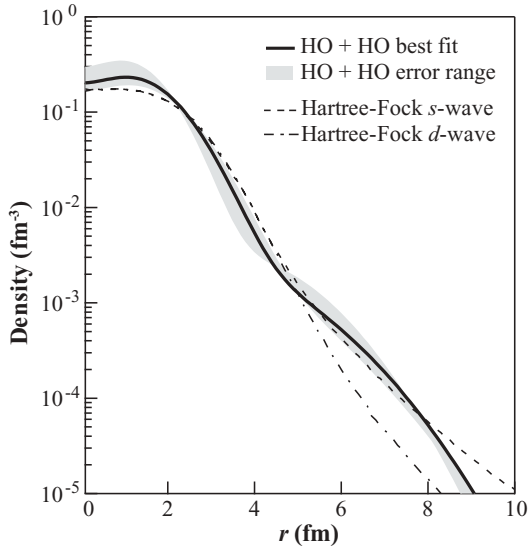

FIG. 8. Density distribution of ^{17}Ne deduced with the fitting procedure assuming an (HO + HO) function. The thick-solid line denotes the best-fit density and the shaded area indicates the error. The other lines show the same theoretical calculations as in Figs. 5 and 6.

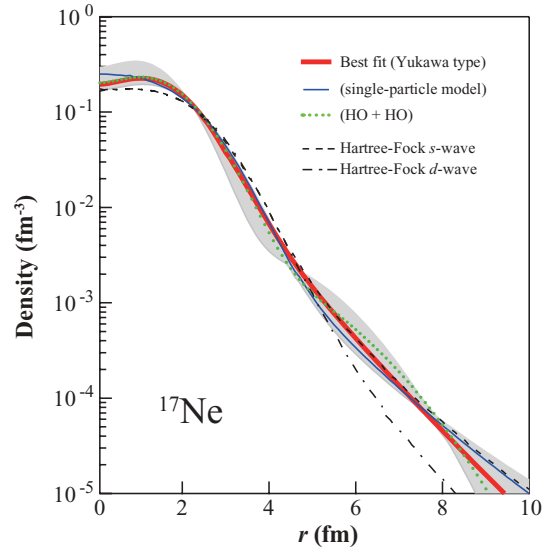

FIG. 9. (Color online) Density distribution of ^{17}Ne in which all the deduced densities and their errors are integrated. The thick-solid line denotes the best-fit density with the (HO + Yukawa-type) function, and the thin-solid line shows that with the (HO + SPM) function. The dotted line indicates the distribution using the (HO + HO) function. The dashed- and dot-dashed lines show the theoretical densities calculated with the Hartree-Fock model with $(2s_{1/2})^2$ and $(1d_{5/2})^2$ configurations, respectively [17].

written as

$$\rho^p(r) = \rho_c^p(r) + \rho_v^p(r)$$
$$\rho_v^p(r) = \left(1 + \eta\left(\frac{r}{b_v}\right)^4\right)\exp\left(-\left(\frac{r}{b_v}\right)^2\right), \quad (14)$$

where $\rho_c^p(r)$ is the core density of HO function for p-shell nuclei shown by Eq. (7) and the density for valence protons in the sd shell is taken to be $\rho_v^p(r)$. For the valence part, the $2s$ orbital is approximated by the first term and the $1d$ orbital is represented by the second term. Thus the parameter η roughly represents the relative strength of the $1d$ orbital. The integral of this valence part was normalized to be two nucleons. The free parameters in this (HO + HO) function are core width b_c, valence width b_v and relative d-orbital amplitude η. The optimized parameters obtained from the χ^2 fitting are $b_c = 1.55$ fm, $b_v = 2.93$ fm, and $\eta = 0.17$. The reduced χ^2 is 0.97 for the (HO + HO) model. Figure 8 shows the deduced density with the (HO + HO) model. The deduced density agrees with the $(2s_{1/2})^2$ theoretical curve in the region with $r = 5 \sim 8$ fm, though it departs from the $(2s_{1/2})^2$ theoretical curve as r increases in the region with $r > 8$ fm because of the functional shape of the (HO + HO) model. This seems to indicate insensitivity of the data to the dilute density in the region with $r > 8$ fm. Therefore, this result dose not contradict the results with the other two density shapes.

4. Summary of the density distribution

Figure 9 shows the density distribution deduced using the three models described above. The error range shown in this figure is taken to be the summed area of the errors in these models. Considering the several types of density shapes, the final deduced density agrees well with the modified HF calculation with the $(2s_{1/2})^2$ configuration, which shows a halo-like tail in the outer region of the core. The present result supports the result from the study on longitudinal momentum distribution and σ_{-2p} [8,9]. The root-mean-square radius of the nucleon distribution in ^{17}Ne was deduced for the best-fit density with a (HO + Yukawa) function to be 1.68 ± 0.06 fm, consistent with the results using the other two functional shapes. This value is also consistent with those in the former works [5,34].

C. Possible shell-structure change on the proton-rich side

In weakly bound neutron-rich nuclei near the drip line, as shown in Ref. [35], energies of levels with lower l, especially with $l = 0$, exhibit less shift relative to the bottom of the potential when the potential depth is varied, due to the large radius of the potential at small binding energies. On the other hand the level energy of the d orbital shifts more rapidly owing to the narrower potential radius caused by the steeper potential wall due to the centrifugal barrier. This difference could lead to the level inversion and the new magic number $N = 16$ for nuclei near the neutron drip-line.

When the valence neutron is bound weakly in a neutron-rich nucleus, the energy shift of the $2s_{1/2}$ level as the depth of the potential becomes shallower is smaller than that for a deeply bound stable nucleus, because the radius of the potential for the valence neutron near zero binding energy in a neutron-rich nucleus is much larger than that in a stable nucleus. In the case of the $1d_{5/2}$ level, however, the centrifugal barrier prevents the potential radius from increasing rapidly as the binding energy decreases near zero binding energy. Thus the shift of the $1d_{5/2}$ level as the depth of potential becomes shallower is

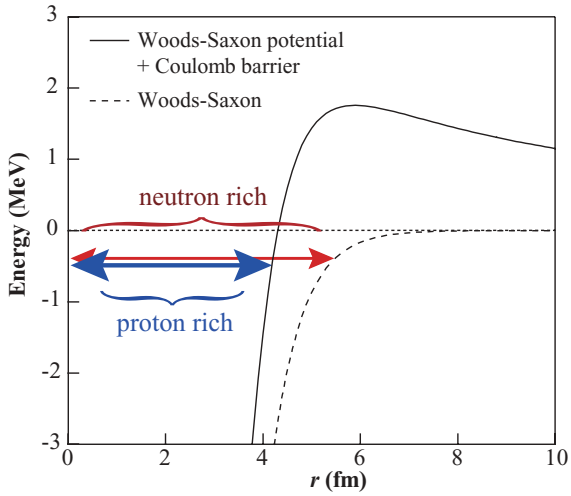

FIG. 10. (Color online) Effect of the Coulomb barrier with the Woods-Saxon potential on a valence nucleon near zero energy for the case of ^{15}O core + $p(n)$ in the $2s_{1/2}$ orbital. If the valence nucleon is a neutron, the width of the Woods-Saxon potential extends rapidly as the energy becomes nearly zero (dashed line). On the contrary, if the valence nucleon is a proton, which leads to the addition of the Coulomb barrier (solid line), the extension of the potential near zero energy is limited.

fairly large, similar to those for stable nuclei, in contrast to the case for the $2s_{1/2}$ level. In the case of proton-rich nuclei, this increase of potential radius near zero energy is hindered by the Coulomb barrier, as shown in Fig. 10. Therefore even for the proton $2s_{1/2}$ level, the energy relative to the potential minimum does not decrease strongly as the potential becomes shallower compared with the case for the neutron $2s_{1/2}$ level in neutron-rich nuclei. Thus, the inversion of the proton $2s_{1/2}$ and $1d_{5/2}$ levels might not readily occur. We therefore quantitatively investigated the possibility of this kind of change in the single-particle level structure for the s and d orbitals in proton-rich nuclei.

A single particle model (SPM) calculation was used to test the inversion of the s and d levels. The level energies of the s and d levels can be obtained using the Woods-Saxon potential shown in Eq. (10) and the Coulomb and the centrifugal barriers. By changing the depth of potential, level energies of the $2s_{1/2}$ and $1d_{5/2}$ in ^{17}Ne were calculated and plotted as a function of potential depth in Fig. 11. In this model, it was assumed that in ^{17}Ne the two protons were bound independently in the ^{15}O potential. With the standard parameters $a = 0.6$ fm and $r_0 = 1.2$ fm, the s and d levels intersect at $S_p = 0.2$ MeV and the level inversion occurs when S_p is less than 0.2 MeV as shown in Fig. 11(A). If the diffuseness of the potential is larger, this level inversion occurs easily even with larger S_p. For instance, in the case of a larger diffuseness $a = 0.8$ fm shown in Fig. 11(A), the $2s_{1/2}$ level is still lower than $1d_{5/2}$ level when it is bound deeply as much as $S_p = 7$ MeV. On the other hand, when the r_0 parameter is smaller than the standard value of $r_0 = 1.2$ fm, the level inversion is also found to occur even at larger S_p as shown in Fig. 11(B). Thus the level energy at which level inversion occurs depends on the diffuseness and radius parameters, a and r_0.

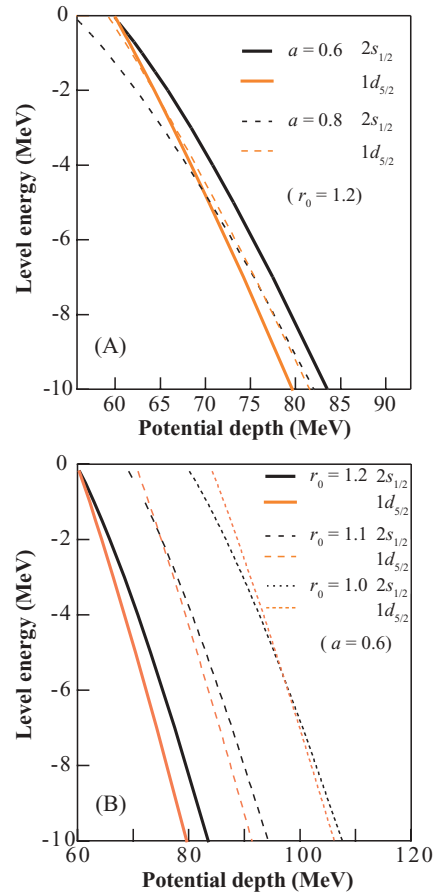

FIG. 11. (Color online) Level energies of $2s_{1/2}$ and $1d_{5/2}$ orbitals are plotted against the potential depth. These are calculated with the Woods-Saxon potential indicated in Eq. (10) plus the Coulomb potential for one valence proton bound on ^{15}O core. If these two levels cross each other at a deep enough energy, the level inversion of $2s_{1/2}$ and $1d_{5/2}$ occurs. (A) shows the diffuseness parameter (a) dependence with a fixed radius $r_0 = 1.2$ fm of the Woods-Saxon potential, and (B) the radius (r_0) dependence with a fixed diffuseness $a = 0.6$ fm.

Figure 12 shows the diffuseness dependence of level energy of the intersection of the $2s_{1/2}$ and $1d_{5/2}$ levels for the proton drip-line and near-drip-line nuclei ^{17}Ne, ^{17}F, ^{20}Na, ^{20}Mg, ^{22}Al, and ^{23}Al. The calculations were done for cases with several different r_0 values. The plotted symbols indicate intersection points of the s and d levels and the solid lines are to guide the eye.

The large closed triangle in Fig. 12 indicates the potential parameters which were deduced by unfolding the proton size from the charge density determined by electron scattering. For the case of ^{17}Ne, the potential parameters for the core nucleus ^{15}O were taken from the charge density of the mirror nucleus ^{15}N, assuming mirror symmetry and the identical-parameter distributions of protons and neutrons for deeply bound mirror nuclei. The parameters used for the core of ^{17}Ne are $a = 0.472(5)$ fm and $r_0 = 0.904(14)$ fm, which are indicated by the large closed triangle in Fig. 12(A). This means that in the region where S_p is less than the binding energy for the triangle (2.4 MeV), the $2s_{1/2}$ level becomes lower in energy than the $1d_{5/2}$ level. As seen in the figure, the experimental S_p, which

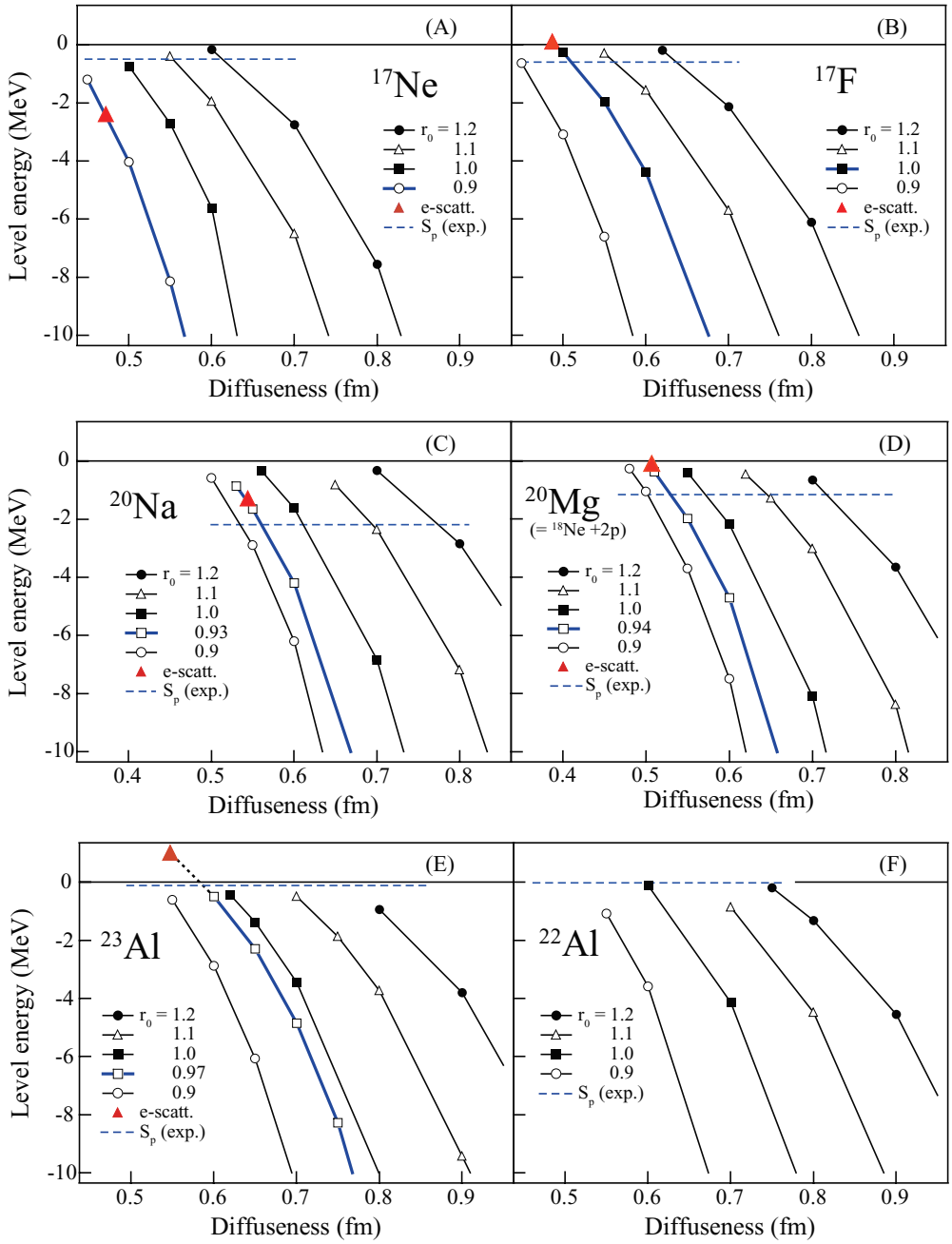

FIG. 12. (Color online) Level energies at intersection points of $2s_{1/2}$ and $1d_{5/2}$ levels as shown in Fig. 11 for several proton drip-line/near-drip-line nuclei are plotted as a function of diffuseness. Cases with several different r_0 values are plotted for each nuclide. The dashed line shows the experimental single proton binding energies of actual nuclei. In the ^{17}Ne and ^{20}Mg cases, S_{1p} is defined as $S_{2p}/2$. The large closed triangles come from the electron-scattering charge densities of the assumed core nuclei or the corresponding equivalent nuclei.

is taken as a half of the experimental two-proton separation energy in ^{17}Ne, is indicated by the horizontal dashed line.

Therefore, in this model, the level inversion occurs for the ^{17}Ne case with these potential parameters based on the electron scattering data. This is consistent with the present experimental result for ^{17}Ne. On the other hand, in the case of ^{17}F, the values of potential parameters similarly deduced from the electron scattering data [36] for the core nucleus ^{16}O are $a = 0.487(5)$ fm and $r_0 = 0.999(14)$ fm. These values are indicated by the large closed triangle in Fig. 12(B). Therefore, the experimental S_p indicated by the dashed line is in the region where the $1d_{5/2}$ level is lower in energy than the $2s_{1/2}$ level. This means that the level inversion does not occur in this case with the present SPM. This fact is quite consistent with that the valence proton in ^{17}F is considered to be in the $1d_{5/2}$ level [$I^\pi(^{17}\mathrm{F}) = 5/2^+$].

The case for ^{20}Na is shown in Fig. 12(C). In this case, the parameters for the potential of the core nucleus ^{19}Ne were deduced from the electron scattering data for the mirror nucleus ^{19}F, similar to the ^{17}Ne case. Both ^{19}Ne and ^{19}F are also deeply

bound nuclei. As shown in the figure, the large closed triangle that indicates these parameters is in the region where the level energy of $1d_{5/2}$ is lower than that of $2s_{1/2}$ as in ^{17}F. Therefore, the level inversion should not take place in this case either. This is also consistent with the experimental spin-parity $I^\pi = 2^+$ of the ground state of ^{20}Na for the following reason. The valence neutron in ^{20}Na is considered to be in $2s_{1/2}$ because the spin-parity of the core nucleus ^{19}Ne is $I^\pi = 1/2^+$ and the magnetic moment of ^{19}Ne, $\mu(^{19}\text{Ne}) = -1.88542(8)$ n.m. [37], is very close to the Schmidt value for a neutron in $2s_{1/2}$. On the other hand, ^{19}F, the mirror nucleus of ^{19}Ne, was found to be deformed with the quadrupole deformation parameter $\beta_2 = 0.41$ [38]. If this deformation is also applicable to the mirror nucleus ^{19}Ne, this prolate deformation creates the proton Nilsson orbital of $3/2[211]$ from the $1d_{5/2}$ spherical orbital. This proton spin of $3/2$ of the Nilsson orbital occupied by the valence proton in ^{20}Na can couple with the neutron $2s_{1/2}$ to form $I^\pi = 2^+$ which is consistent with the experimental value. These consistencies also support the plausibility of the present simple SPM.

Figure 12(D) shows the case for ^{20}Mg. In this case, potential parameters for the core nucleus ^{18}Ne were taken from the electron-scattering data for the mirror nucleus ^{18}O, similar to the cases for ^{17}Ne and ^{20}Na. This figure indicates that the level inversion does not take place in ^{20}Mg. In order to assess the consistency of this result, we consider the mirror system of $^{18}\text{O} + n$, i.e., ^{19}O, instead of $^{18}\text{Ne} + p$ system because it is not bound. Because the ground state spin-parity of ^{19}O is $5/2^+$, the valence neutron in ^{19}O is considered to be in $1d_{5/2}$. This is consistent with the above result for ^{20}Mg.

The ^{23}Al and ^{22}Al cases are shown in Figs. 12(E), and 12(F). For ^{23}Al, the parameters from electron scattering are indicated by the large closed triangle in Fig. 12(E). These were taken from the potential parameters of ^{22}Ne, which is the mirror of the core nucleus ^{22}Mg. This figure shows that s-d level inversion does not occur in ^{23}Al, which is also consistent with the experimental spin value of $5/2$ [39]. On the other hand in the case of ^{22}Al shown in Fig. 12(F), because information on the potential parameters for the core nucleus ^{21}Mg or the mirror nucleus ^{21}F does not exist, we cannot specify an experimental point in the figure and cannot judge whether the level inversion should occur. If the parameters are the same as those for ^{23}Al, the level inversion does not occur in ^{22}Al. However, if the radius parameter r_0 is somewhat smaller or the diffuseness a is a little larger compared to those for ^{23}Al, the level inversion takes place within the reasonable range of parameters.

As described above, the simple single particle model seems to simulate the s-d level inversion very well. Thus, at present, ^{17}Ne might be the only proton drip-line nucleus for which the s-d level inversion takes place on the proton-rich side in the sd shell. The drip-line nucleus ^{22}Al is also interesting for future investigation.

V. SUMMARY

We measured reaction cross sections for ^{17}Ne on ^{9}Be, ^{12}C, and ^{27}Al targets at 64 and 42 MeV/nucleon through the transmission method. Since the σ_R becomes sensitive to the dilute density part at lower beam energies, we deduced the density distribution of ^{17}Ne by the energy dependence of σ_R through fitting procedures using a Glauber-type calculation.

To deduce an accurate density distribution, we applied a Glauber calculation in which the higher-order multiple scattering effect and the Fermi-motion effect were taken into account. ^{17}Ne was found to have a halo-like dilute tail in the density distribution, consistent with the $(2s_{1/2})^2$ configuration for valence protons. Since in a naive picture the valence protons should have the $(1d_{5/2})^2$ configuration, this result supports a change in the shell structure in the sd-shell region for proton rich nuclei. With the simple single particle model calculation, level inversions in ^{17}Ne and neighboring proton rich nuclei can be understood using the known electron-scattering parameters for core nuclei. However, according to the simple calculation, ^{17}Ne might be the only case, at present, in which level inversion occurs in a proton rich nucleus.

ACKNOWLEDGMENTS

The authors gratefully acknowledge all of the staff at the RIKEN ring cyclotron for their operation of the accelerator during the experiment. The authors would also like to thank Dr. Jack Miller at Lawrence Berkeley National Laboratory for his careful reading of the manuscript. This work was partially supported by the Grant-in-Aid for Scientific Research (C) from the Japan Society for the Promotion of Science.

[1] T. Minamisono *et al.*, Phys. Rev. Lett. **69**, 2058 (1992).
[2] W. Schwab *et al.*, Z. Phys. A **350**, 283 (1995).
[3] J. Kelley *et al.*, Phys. Rev. Lett. **77**, 5020 (1996).
[4] M. Fukuda *et al.*, Nucl. Phys. A **656**, 209 (1999), and references therein.
[5] A. Ozawa *et al.*, Phys. Lett. B **334**, 18 (1994).
[6] M. J. G. Borge *et al.*, Phys. Lett. B **317**, 25 (1993).
[7] R. Warner *et al.*, Nucl. Phys. A **635**, 292 (1998).
[8] R. Kanungo *et al.*, Phys. Lett. B **571**, 21 (2003).
[9] R. Kanungo, Nucl. Phys. A **734**, 337 (2004).
[10] W. Geithner *et al.*, Phys. Rev. Lett. **101**, 252502 (2008).
[11] N. K. Timofeyuk, P. Descouvemont, and D. Baye, Nucl. Phys. A **600**, 1 (1996).
[12] E. Garrido, D. V. Fedorov, and A. S. Jensen, Phys. Rev. C **69**, 024002 (2004).
[13] E. Garrido, D. V. Fedorov, and A. S. Jensen, Nucl. Phys. A **733**, 85 (2004).
[14] S. Nakamura, V. Guimarães, and S. Kubono, Phys. Lett. B **416**, 1 (1998).
[15] H. T. Fortune and R. Sherr, Phys. Lett. B **503**, 70 (2001).
[16] H. T. Fortune, R. Sherr, and B. A. Brown, Phys. Rev. C **73**, 064310 (2006).
[17] H. Kitagawa, N. Tajima, and H. Sagawa, Z. Phys. A **358**, 381 (1997).
[18] T. Otsuka, R. Fujimoto, Y. Utsuno, B. A. Brown, M. Honma, and T. Mizusaki, Phys. Rev. Lett. **87**, 082502 (2001).

[19] A. Ozawa, T. Kobayashi, T. Suzuki, K. Yoshida, and I. Tanihata, Phys. Rev. Lett. **84**, 5493 (2000).
[20] K. Hagiwara *et al.* (Particle Data Group), Phys. Rev. D **66**, 010001 (2002).
[21] T. Kubo *et al.*, Nucl. Instrum. Methods Phys. Res., Sect. B **70**, 309 (1992).
[22] H. Kumagai *et al.*, Nucl. Instrum. Methods Phys. Res., Sect. A **470**, 562 (2001).
[23] S. Kox *et al.*, Phys. Rev. C **35**, 1678 (1987).
[24] M. Takechi *et al.*, Phys. Rev. C **79**, 061601(R) (2009).
[25] B. Abu Ibrahim and Y. Suzuki, Phys. Rev. C **61**, 051601(R) (2000).
[26] Y. Suzuki, H. Matsumura, and B. Abu-Ibrahim, Phys. Rev. C **70**, 051302(R) (2004).
[27] H. Jeppesen *et al.*, Nucl. Phys. A **739**, 57 (2004).
[28] M. Fukuda *et al.*, Phys. Lett. B **268**, 339 (1991).
[29] H. Y. Zhang *et al.*, Nucl. Phys. A **707**, 303 (2002).
[30] D. Q. Fang *et al.*, Phys. Rev. C **69**, 034613 (2004).
[31] Y. Yamaguchi *et al.*, Phys. Rev. C **70**, 054320 (2004).
[32] A. Ozawa, Nucl. Phys. A **738**, 38 (2004).
[33] A. Bohr and B. R. Mottelson, *Nuclear Structure*, Vol. I (Benjamin, New York, 1975).
[34] C. A. Bertulani and M. S. Hussein, Phys. Rev. C **76**, 051602(R) (2007).
[35] I. Hamamoto, Nucl. Phys. A **731**, 211 (2004).
[36] H. DeVries, C. DeJager, and C. DeVries, At. Data Nucl. Data Tables **36**, 495 (1987).
[37] R. Firestone, V. Shirley, C. Baglin, S. Chu, and J. Zipkin, *Table of Isotopes*, 8th ed. (Wiley Interscience, New York, 1996).
[38] P. L. Hallowell *et al.*, Phys. Rev. C **7**, 1396 (1973).
[39] A. Ozawa *et al.*, Phys. Rev. C **74**, 021301(R) (2006).